

# A hybrid Eulerian-Lagrangian model for spectral wave evolution with application to bottom friction on the continental shelf

Fabrice Ardhuin\*, T. H. C. Herbers and W. C. O'Reilly  
Department of Oceanography, Naval Postgraduate School, Monterey,  
CA, 93943-5122, USA

October 10, 2000

## Abstract

A hybrid Eulerian-Lagrangian wave model is presented that solves the spectral energy balance equation for surface gravity waves in varying depth. The energy of each spectral component is advected along (Lagrangian) ray trajectories. The source terms in the energy balance equation (e.g. interactions between wave components and non-conservative processes) are computed on a fixed Eulerian grid and interpolated onto the ray trajectories. The source terms are integrated in time along the rays. This integration is performed in parallel over the entire model domain. The main advantage of this new model, named CREST (Coupled Rays with Eulerian Source Terms), is that refraction of waves by subgrid-scale depths variations is evaluated accurately using pre-computed rays, and thus the model can be applied with relatively coarse source term grids to large coastal areas. Hindcasts of swell evolution across the North Carolina continental shelf are presented for a source term restricted to energy dissipation in the bottom boundary layer over a movable sandy sea bed. The results show that the hybrid Eulerian-Lagrangian method is a viable approach for accurate wave predictions in large coastal regions with nonstationary boundary conditions. Good agreement between model predictions and field observations of swell decay supports the hypothesis that, in the absence of strong local wind forcing, the evolution of waves across a wide, sandy continental shelf is dominated by refraction and bottom friction, which is well represented by a moveable bed parameterization.

## 1. INTRODUCTION

In shallow water, surface gravity waves are affected by sea bed features with a wide range of scales. Wave refraction over large scale (nominally 1 to 10 km) bottom features can induce dramatic variations in wave energy along the coast that are readily observed

---

\*Also at Service Hydrographique et Océanographique de la Marine, Brest, France

(e.g. Munk and Traylor, 1947). The effects of refraction on the evolution of wave spectra are generally well understood, and accurately predicted by geometrical optics models (e.g. Longuet-Higgins, 1957; O'Reilly and Guza, 1993). Smaller scale (one half to several wavelengths) bottom features can scatter waves, possibly causing increased directional spreading of waves on the continental shelf, and reduced wave heights near the shore. Models for this process exist (e.g. Long, 1973) but concurrent observations of wave evolution and fine scale bathymetry data are not yet available to assess the importance of this mechanism.

In addition to these relatively well understood energy conserving wave-bottom interaction processes, wave evolution across continental shelves and in shallow marginal seas is also believed to be strongly affected by non-conservative bottom boundary layer processes (e.g. Shemdin et al., 1980; Bouws and Komen, 1983; Weber, 1988; Young and Gorman, 1995). For sea beds composed of non-cohesive sandy sediments, the dissipation of wave energy in the bottom boundary layer is strongly dependent on the presence of sand ripples formed by the near-bed wave orbital motion. Neglecting currents unrelated to the waves, the bottom boundary layer can be classified in three regimes, based on the ratio of friction and buoyant forces acting on a sand grain, and represented by the Shields number  $\psi$  (e.g. Nielsen, 1981). For small values of  $\psi$ , the bottom morphology does not change, thus retaining the history of past wave events and biological activity. In this 'relict roughness' regime wave energy dissipation is minimal as bottom velocities are small and turbulence is weak. As  $\psi$  increases past a threshold value  $\psi_c$  (typically 0.05 for well-sorted quartz sand) the wave flow intermittently moves surficial sediments that organize into ripple fields (e.g. Nielsen, 1981; Traykovski et al., 1999). These 'active ripples' sharply increase the turbulent dissipation of wave energy as vortices are shed by the orbital flow at the ripple crests. According to Madsen et al. (1990) the drag coefficient for spectral wave motion over ripples is maximum for  $\psi \simeq 1.2\psi_c$ . Example swell conditions with this maximum drag are a peak period  $T_p=12$  s, and significant wave height  $H_s = 1.5$  m in 25 m depth over well sorted quartz sand with grain size  $D = 0.15$  mm. For larger values of  $\psi$  the drag coefficient decreases as ripples are eroded. For very large values of  $\psi$  (typically  $\psi \sim 20\psi_c$ , corresponding to  $H_s = 5$  m keeping the other parameters unchanged) ripples are obliterated and a layer of sediments moves with the water column (e.g. Li and Amos, 1999). Both the thickness of this 'sheet flow' layer and the drag coefficient increase with  $\psi$ .

Models for the evolution of waves over a movable sandy bed (e.g. Graber and Madsen, 1988; Tolman, 1994) usually involve a 'ripple roughness predictor' which, based on the wave conditions and sediment nature, determines the flow regime, the type of bottom features (e.g. Clifton, 1976; Wiberg and Harris, 1995) and their equivalent sand grain roughness  $k_N$  (e.g. Grant and Madsen, 1982; Madsen et al. 1990; Li and Amos 1998, 1999). This roughness predictor is combined with a hydrodynamic model of the bottom boundary layer flow that predicts the corresponding wave energy dissipation. Most hydrodynamic models parameterize turbulence with a vertical profile of the eddy viscosity (Kajiura, 1968; Grant and Madsen, 1979; Weber, 1991a, 1991b; see Wiberg, 1995, for a review). The use of a single roughness length for spectral waves was validated in laboratory experiments by Mathisen and Madsen (1999).

Most numerical models for the evolution of surface gravity waves across ocean basins, marginal seas, and continental shelves that account for non-conservative processes are

based on a spectral energy balance (Gelci et al., 1957). The wave field can be represented by the spectral energy densities  $F(\underline{x}, \underline{k}, t)$ , in wavenumber space ( $\underline{k}$ ), as a function of geographical space ( $\underline{x}$ ) and time ( $t$ ). Neglecting currents, the Eulerian energy balance equation is given by (e.g. Whitham 1974):

$$\frac{\partial F}{\partial t} + \nabla_{\underline{x}} \cdot (\underline{c}_g F) + \nabla_{\underline{k}} \cdot (\underline{c}_k F) = S \quad (1)$$

where  $\nabla_{\underline{x}}$  and  $\nabla_{\underline{k}}$  are horizontal divergence operators in geographical and wavenumber space respectively, and  $\underline{c}_g$  (the group speed) and  $\underline{c}_k$  are the corresponding energy transport velocities. The source term  $S(\underline{k}, \underline{x}, t)$  is the net rate of energy transfer to component  $\underline{k}$  resulting from wind forces on the sea surface, dissipation processes (wave breaking, bottom friction) and nonlinear interactions with other components of the spectrum. In most operational wave models the energy balance equation (1) or a similar action balance equation is fully discretized in the 5 dimensional  $(\underline{k}, \underline{x}, t)$  space and integrated in time on a Eulerian grid. These models are widely used in deep water applications where large spatial and temporal scales of wave evolution allow for relatively coarse grids (e.g. The SWAMP group, 1984; Komen et al, 1994).

In shallow water accurate representation of refraction may require grid resolution of the order of 100 m. If the region of interest is small (less than 100 km<sup>2</sup>), a high resolution Eulerian model is feasible and gives good results (Booij et al., 1999), but the computational cost is presently too large for larger shelf areas, even in a steady state formulation. Additionally, finite difference approximations in these models cause numerical diffusion, artificially spreading wave energy in time,  $\underline{x}$ , and  $\underline{k}$  space, in a way unrelated to the physical evolution of a wave spectrum over bottom topography. High-order finite difference schemes and piecewise ray methods, using local ray trajectories to estimate the advection terms of eq. (1), have been developed to mitigate this effect (Sobey, 1986; Young, 1988; Benoit et al., 1996).

The spectral energy balance can also be formulated from a Lagrangian point of view:

$$\frac{dF}{dt} = S \quad (2)$$

where the left-hand side is the rate of change of  $F$  following a wave component along its ray trajectory. Eqs. (1) and (2) are equivalent for waves that obey a dispersion relation of the form  $f = W(\underline{k}, \underline{x}, t)$  where  $f$  is the wave component frequency. However, in contrast to the Eulerian balance (1), the along-ray conservation of spectral densities is valid only in  $\underline{k}$ -space (Longuet-Higgins, 1957). Lagrangian wave prediction models based on (2) usually assume a source term  $S$  equal to zero. This approach is suitable for narrow shelf regions where propagation distances are too short for significant wave generation or decay (O'Reilly and Guza, 1991). Lagrangian models avoid the numerical diffusion of finite difference schemes, but the ray trajectories are highly sensitive to topography details. The scattering of rays over rough bottom topography causes physical diffusion of wave energy that may broaden wave spectra in shallow water. The accurate representation of these fine scale bathymetry effects in a ray model requires averaging over a large number of rays, whether the rays be computed from initially parallel directions (forward refraction, e.g. Bouws and Battjes, 1982) or from fixed points (back-refraction, e.g. O'Reilly and Guza, 1993). Back-refraction models are not based on finite area elements, unlike forward

refraction and finite-difference schemes in Eulerian models, and thus have different conservation properties. For example finite-difference schemes are generally constrained to conserve energy fluxes through the model domain, but the energy fluxes obtained through spatial interpolation in a back-refraction model balance exactly only in the limit of high spatial and wavenumber resolution. Nevertheless if resolution bathymetry is available, a back-refraction ray model with high wavenumber resolution gives a potentially more accurate representation of wave propagation than finite difference schemes.

Cavaleri and Malanotte Rizzoli (1981) included wind input and dissipation source terms in a ray model. Their model parameterizes the source terms for each individual wave component, and solves the energy balance equation independently for each ray, without any coupling. In this study we include coupling between rays through a source term that is parameterized in terms of the full energy spectrum. The source term  $S(\underline{k}, t)$  is evaluated at each point of a coarse Eulerian grid, and subsequently interpolated from this grid onto ray trajectories. The energy balance equation (2) is solved along a full spectrum of rays traced backward from each grid point to the model boundary. Spectral components are advected from the model boundary along the precomputed rays while being modified by the interpolated source terms, until they reach a grid point where all components are combined into a full spectrum  $F(\underline{k}, t)$  from which  $S(\underline{k}, t)$  can be evaluated. The advection and source term computations are performed simultaneously for the entire model domain. This hybrid Eulerian-Lagrangian model essentially couples a Lagrangian energy advection scheme with an Eulerian source term computation scheme. The formulation of the source term computations is not constrained in any way by the advection scheme and thus can be adapted from existing third-generation models.

In section 2 the details of the numerical model hereinafter referred to as CREST (Coupled Rays with Eulerian Source Term), are described: ray computations, ray ensemble averaging, source term interpolation, and time integration. The source term, restricted in this paper to Tolman’s (1994) parameterization of wave energy dissipation on a movable sandy bottom, is reviewed in section 3. A numerical implementation of the model for the North Carolina continental shelf is described in section 4. Hindcasts of swell attenuation across the shelf are compared in section 5 to observations from the DUCK94 experiment. The parameterization of bottom friction, and the efficiency of hybrid Eulerian-Lagrangian spectral wave models are discussed in section 6, followed by a summary in section 7.

## 2. NUMERICAL SCHEMES

The model consists of two parts. First wave rays are traced backwards from fixed Eulerian grid points with positions  $\underline{x}_i$  to the model boundary. Second, these trajectories are used to integrate eq. (2) in time, using an ensemble average over a large number of rays. Along each ray, arriving at  $\underline{x}_i$  with a wavenumber vector  $\underline{k}$ , we define a Lagrangian energy density  $F^L(t, \tau)$  as the energy density ‘upstream’ of  $\underline{x}_i$  at time  $t$ , where  $\tau$  is the energy advection time from the local ray position to the grid point  $\underline{x}_i$ . The spectral densities  $F^L$  are averaged over ensembles of rays within finite bands  $\underline{k}_j$  of the arrival wavenumbers  $\underline{k}$  at  $\underline{x}_i$ . The full Eulerian energy density spectrum  $F^E(\underline{x}_i, \underline{k}, t)$  at  $\underline{x}_i$  is evaluated by combining the average Lagrangian density predictions  $F^L(t, 0)$  at  $\underline{x}_i$  for all bands  $\underline{k}_j$ . A source term  $S(\underline{x}_i, \underline{k}_j, t)$  is determined at each grid point from the full Eulerian spectrum  $F^E$  and other

local parameters (e.g. wind stress and bottom roughness).  $S$  is then interpolated in  $\underline{x}$  and  $\underline{k}$  space to yield an approximate source term  $\tilde{S}(t, \tau)$  at the local ray positions and wavenumbers which in turn modifies  $F^L(t, \tau)$  along the rays (Figure 1). Rays and grid

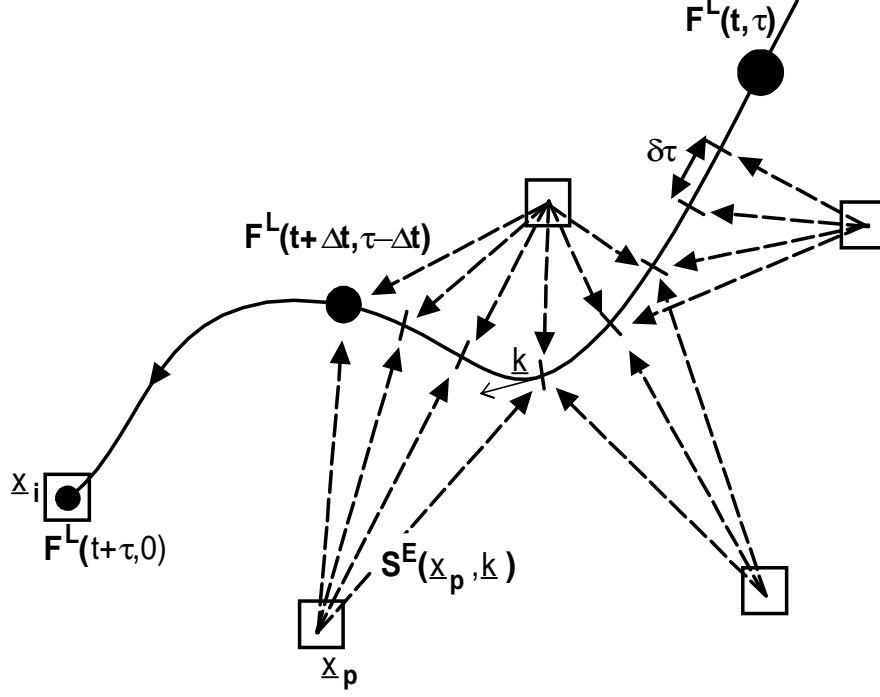


FIG. 1. Schematic of the integration of the Lagrangian energy balance equation from  $t$  to  $t + \Delta t$  along a single ray (solid curve) using a spatially interpolated source term. Filled circles symbolize the magnitude of the energy density, and dashed arrows indicate the interpolation of the source term from the Eulerian grid (squares) onto the ray at increments  $\delta\tau$ . See section 2 for further details.

are thus coupled at  $\tau = 0$  only.

The entire set of interpolation coefficients, representing the influence of the topography on waves is precomputed once, and stored in files. Using these files and a time series of wave spectra at the model open boundaries the energy balance equation is integrated in time.

Although the Lagrangian energy balance (2) holds only for energy density in wavenumber ( $\underline{k}$ ) space, the propagation of waves is formulated more conveniently using wave frequency  $f$  and direction  $\theta$  as variables. In the following  $f$  and  $\theta$  are used throughout in ray calculations, grid discretization and result displays, but the energy density in  $\underline{k}$  space

is used in the energy balance calculations.

### a. Model domain and boundary conditions

The model domain covers a region of known bottom topography. From an arbitrary set of  $N_{gp}$  grid points (hereinafter called ‘model grid’) with locations  $(\underline{x}_i)_{i=1, N_{gp}}$  a triangular mesh is generated using Delauney’s tessellation technique. The outermost points of the mesh form the model boundary, which is therefore a polygon. Additional interior polygons can be added to the boundary in order to represent islands in the model domain (Figure 2) \. Ray trajectories are traced backward in time from the grid points  $\underline{x}_i$  until they cross a boundary. For each  $\underline{x}_i$ , rays are computed for a large number of frequencies  $f_j$  and arrival directions  $\theta_l$ . Depending on the geographical region covered by the model domain, rays can be trapped in shallow water and end at the coast, or reach a deep water region where they become straight, or cross the model boundary in a region of intermediate depth. In all cases a ray is terminated when it crosses a triangle side connecting two boundary grid points, and the Lagrangian energy density carried by the ray into the model domain is approximated by a linear interpolation of the spectral densities at these two grid points (Figure 2).

The boundary condition for the model is therefore fully prescribed by the spectral densities at the grid points along the boundary, for directions toward the inside of the boundary. On the open part of the boundary, spectra may be estimated from deep water wave measurements or obtained by nesting the model within a larger scale wave model. On the closed coastal part of the boundary, the energy entering the domain may be set equal to zero (i.e. wave energy impinging on the coast is dissipated in the surf zone) or, in the case of a steep coastline, determined by partially reflecting the shoreward energy flux. In order to reduce the scattering of rays over large propagation distances, the model domain can be subdivided into subdomains that are coupled through their common boundaries. This technique reduces memory requirements by shortening the rays, at the expense of some local numerical diffusion, as the energy that is transmitted through the boundary is interpolated from boundary grid points (e.g. ray d in figure 2).

### b. Precomputations

#### 1) Rays.—

In applications presented here the model domain is small enough to neglect the curvature of the earth, and use local Cartesian  $(x, y)$  coordinates. The geometry of wave rays is determined by Fermat’s geometrical optics principle that the integral of the phase speed  $c$  along a curve is minimum when this curve is a ray, which yields Snel’s law when bottom contours are parallel. The ray equations are:

$$\frac{dx}{ds} = \cos(\theta) \quad (3a)$$

$$\frac{dy}{ds} = \sin(\theta) \quad (3b)$$

$$\frac{d\theta}{ds} = \frac{1}{c} \frac{dc}{dh} \left[ \frac{dh}{dx} \cdot \sin(\theta) - \frac{dh}{dy} \cdot \cos(\theta) \right] \quad (3c)$$

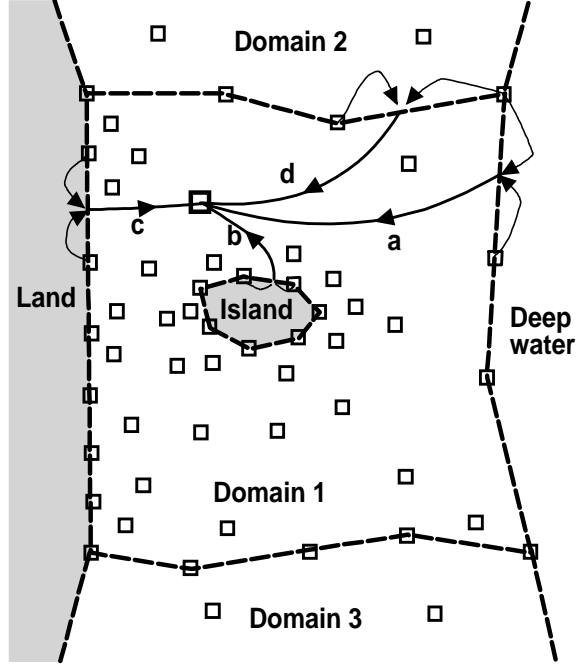


FIG. 2. Schematic of the boundary condition treatment for an arbitrary model grid (squares represent grid points). The boundary (dashed lines) separates and couples adjacent model subdomains. Examples are shown of rays transporting energy into the model domain from four different types of boundaries (a: shelf break, b: island, c: coast, d: internal boundary between model subdomains) to a given grid point (large square). In cases a and d energy is advected through the boundary, whereas in cases b and c energy is reflected from the boundary. In all cases, the energy is interpolated (dotted arrows) at the boundary from the adjacent two boundary grid points.

with  $s$  a curvilinear coordinate along the ray,  $h$  the water depth, and  $\theta$  the angle between the  $x$  axis and the tangent to the ray. Wave energy is transported along the ray with the group velocity  $c_g$  and the frequency  $f$  is conserved. In the linear approximation we have:

$$(2\pi f)^2 = gk \tanh(kh) \quad (4a)$$

$$c = \sqrt{\frac{g}{k} \tanh(kh)} \quad (4b)$$

$$c_g = c \left( \frac{1}{2} + \frac{kh}{\sinh(2kh)} \right) \quad (4c)$$

where  $k = |\underline{k}|$  is the wavenumber magnitude.

Along the ray the local depth and bottom slopes are evaluated from a biquadric fit to the bathymetry grid (Dobson, 1967). The wavenumber magnitude  $k$  is computed from  $f$  using eq. (4a) and used to determine  $c$ ,  $c_g$  and  $\frac{dc}{dh}$ . With these parameters eqs. (3) are integrated using an error-controlled Cash-Karp Runge-Kutta scheme (Press et al., 1992) with a variable step size.

Along each ray the position and direction  $(\underline{x}^m, \theta^m)$  are computed at small distance intervals  $\delta s = \int_{\tau^m}^{\tau^m + \delta\tau} c_g d\tau$  that correspond to a fixed advection time step  $\delta\tau$ . A  $\delta\tau$  was chosen for each frequency such that  $\delta s = 200$  m in deep water. The result of the ray computation is a series of positions and directions  $(\underline{x}^m, \theta^m)$  for each of the rays with  $m$  ranging from 0 at the initial grid point to  $M$  at the domain boundary, with typical values  $M \sim 1000$  in the implementation presented in section 4.

$M$ ,  $\underline{x}^M$  and  $\theta^M$  give the time lag, position and direction at the end of the ray, needed to specify the boundary condition. Although waves can travel along the same ray in both directions, the rays are used here only to advect energy from the boundaries to the grid points.

## 2) Interpolation of boundary conditions and source term.—

At each position  $\underline{x}^m$  along a ray, a local source term estimate  $\tilde{S}(\underline{x}^m)$  is given by the linear interpolation in space of source term predictions at the three grid points  $\underline{x}_i$  of the local triangle. Since the source term is computed only at discrete directions  $\theta_l$ , another linear interpolation, with weights  $w_l^m$ , is performed over the two directions  $\theta_l$  that enclose the local direction  $\theta^m$  of the ray. The same procedure is used for deriving an estimate  $\tilde{F}^B$  of the energy density  $F^L(\tau^M)$  at the boundary:

$$\tilde{S}(\underline{x}^m) = \sum_{i,l} \alpha_i^m w_l^m S(\underline{x}_i, \theta_l) \quad (5a)$$

$$\tilde{F}_B = \sum_{i,l} \beta_i w_l^M F^E(\underline{x}_i, \theta_l) \quad (5b)$$

where the spatial weighting coefficients  $\alpha_i^m$  and  $\beta_i$  are nonzero only for the three grid points  $\underline{x}_i$  on the vertices of the local triangle, and the two points of the boundary segment crossed by the ray, respectively.

In order to resolve the refraction of a single wave component and interpolate accurately the source term onto the ray, a small time step  $\delta\tau$  is required that is of the order of 10



to 100 s for typical swell group velocities ( $c_g = O(10 \text{ m s}^{-1})$ ) and scales ( $O(1 - 10 \text{ km})$ ) of bottom features. This time step is too small for an efficient time integration of the energy balance equation (2). This integration is performed here with a fixed larger time step  $\Delta t$  (10 minutes in the calculations presented here), that resolves the typically slower evolution of the wave energy and source terms in space, and temporal changes of the offshore boundary conditions. The source term  $\tilde{S}$  (Eq. 5a) is averaged over an advection time interval  $\Delta t^n$ , that covers values of  $\tau$  from  $(n - 1) \Delta t$  to  $n \Delta t$ :

$$\tilde{S}^n = \sum_{i,l} A_{il}^n S(\underline{x}_i, \theta_l) \quad (6)$$

$$\text{with } A_{il}^n = \frac{\delta \tau}{\Delta t} \sum_{i'=i, l'=l, m} \alpha_{i'}^m w_{l'}^m \quad (7)$$

where the summation over  $m$  includes all ray segments that fall within the time step  $\Delta t^n$ . In the applications presented here the timestep index  $n$  ranges from 0 at the grid point to 10-50, depending on the location of the grid point, the frequency of the waves, and the complexity of the topography. Higher frequency waves and rough topography require more timesteps than low frequency waves and smooth topography, because the group velocity decreases with increasing frequency and bending of rays over rough topography lengthens the propagation path.

### 3) Finite bandwidth approximation.—

So far we have considered the evolution of the spectral energy density  $F^L(t, \tau)$  along a single ray. Since individual ray trajectories are highly sensitive to the underlying bathymetry, the energy balance equation is ensemble-averaged over a ‘bundle’ of rays originating from  $\underline{x}_i$  with frequencies and directions covering a small but finite bandwidth. The rays that form a bundle can be scattered and follow different paths away from  $\underline{x}_i$ , therefore the ray ensemble has a physical interpretation only at the grid points  $\underline{x}_i$  as a finite bandwidth average. The ensemble averaged energy density  $F^L$  and associated source term interpolation coefficients  $A_{il}^n$  are given by weighed averages of single-ray values:

$$F^L(t, \tau) = \sum_r b_r F_r^L(t, \tau) \quad (8a)$$

$$A_{il}^n = \sum_r b_r A_{il}^{r,n} \quad (8b)$$

where the summation is over all the rays in the bundle, and  $b_r$  is the fraction of the finite bandwidth attributed to the individual ray  $r$ .

Different rays from the same bundle may reach the boundary during different timesteps, so that the ensemble average ‘boundary energy’  $\tilde{F}_B^n$  must be defined for each time step  $n$ :

$$\tilde{F}_B^n = \sum_{i,l} B_{il}^n F^E(\underline{x}_i, \theta_l) \quad (9a)$$

$$B_{il}^n = \sum_{r, i'=i, l'=l} b_r \beta_{i'}^r w_{l'}^{r,M} \quad (9b)$$

where the summation is restricted to those rays that reach the boundary during time step  $n$ .

Averaging over finite frequency-direction bands not only accounts for the scattering of rays by refraction over bottom irregularities, but also has the advantage of avoiding the ‘garden sprinkler effect’ of Eulerian models formulated for a discrete spectrum (e.g. SWAMP group, 1984). A large number of ray computations (of the order of 1000 for applications presented here) may be needed to obtain a stable ensemble average but these time-consuming computations can be performed in parallel for different bundles and grid points.

The results of the precomputation are the ensemble averaged interpolation coefficients  $A_{il}^n$  and  $B_{il}^n$ . These coefficients are written to files that are used in the time-integration scheme described below.

### c. Integration in time

The energy balance equation (2), averaged over ray ensembles, is a unidimensional time evolution equation that can be integrated using standard finite difference schemes. However, a more accurate formulation is possible for linear or quasi-linear source terms. The total source term  $S$  is split into a (quasi-)linear part  $\lambda F$  and a residual term  $R$  that includes constant and non-linear (in  $F$ ) contributions:

$$\frac{dF}{dt} = \lambda F + R \quad (10)$$

For  $\lambda$  and  $R$  constants, eq. (10) has an exact solution for the evolution of  $F$  over one time step:

$$F(t + \Delta t) = F(t) \exp(\lambda \Delta t) + R \left[ \frac{\exp(\lambda \Delta t) - 1}{\lambda} \right] \quad (11)$$

For  $\lambda$  and  $R$  varying slowly in time and space an approximate solution is obtained by replacing  $\lambda$  and  $R$  in eq. (11) with average values. The interpolation of the total source term  $\lambda F + R$  is more accurate with this formulation, provided that the gradients of  $\lambda$ , in  $\underline{k}$ -space,  $\underline{x}$ -space and time are smaller than those of  $F$  (see appendix B). For fully non-linear source terms (i.e.  $\lambda = 0$ ) eq. (11) reduces to a first order Euler scheme.

$\lambda$  and  $R$  are assumed to be known functions  $\Omega$  and  $\Theta$  of the local wave spectrum that can be adopted from parameterizations in existing Eulerian models.  $\lambda$  and  $R$  are interpolated from the Eulerian grid onto the rays using the precomputed coefficients  $A_{il}^n$ . The complete integration scheme is given by:

Source term evaluation (on the grid):

$$\lambda(t) = \Omega(F^E(t)) \quad (12a)$$

$$R(t) = \Theta(F^E(t)) \quad (12b)$$

Interpolations (grid to rays coupling):

$$\tilde{F}_B^n(t) = \sum_{i,l} B_{il}^n F^E(\underline{x}_i, \theta_l, t) \quad (12c)$$

$$\tilde{\lambda}^n(t) = \left[ \sum_{i,l} A_{il}^n \lambda(\underline{x}_i, \theta_l, t) F^E(\underline{x}_i, \theta_l, t) \right] / \sum_{i,l} A_{il}^n F^E(\underline{x}_i, \theta_l, t) \quad (12d)$$

$$\tilde{R}^n(t) = \sum_{i,l} A_{il}^n R(\underline{x}_i, \theta_l, t) \quad (12e)$$

Prognostic equation (along the rays):

$$F^L(t + \Delta t, (n-1)\Delta t) = F_B^n(t) + F^L(t, n\Delta t) \exp(\tilde{\lambda}^n(t) \Delta t) + \tilde{R}^n(t) \left[ \frac{\exp(\tilde{\lambda}^n(t) \Delta t) - 1}{\tilde{\lambda}^n(t)} \right] \quad (12f)$$

Rays to grid coupling (at  $\tau = 0$ ):

$$F^E(t + \Delta t) = \begin{cases} F^L(t + \Delta t, 0) \\ \text{or} \\ F_B(t + \Delta t) \end{cases} \quad (12g)$$

where the frequency variable  $f_j$  is omitted. Variables  $\underline{x}_i$ , and  $\theta_l$  are written explicitly only in the interpolations eqs. (12.c,d and e). In eq. (12d) the weighting of  $\lambda$  by the corresponding energy density  $F^E$  allows the conservation of the source term  $\lambda F$  in the interpolation. The prognostic equation (12f) applies the interpolated boundary condition and source term to the Lagrangian energy balance to determine  $F^L$  at the next time step. The Eulerian spectrum  $F^E$  is advanced to time  $t + \Delta t$  with eq. (12g), closing the set of equations. For grid points  $\underline{x}_i$  located on model domain boundaries, the spectral densities  $F^E$  for waves travelling into the model domain are prescribed by the boundary condition  $F_B$ . On the deep water boundary  $F_B$  is set equal to the observed deep water spectrum. At other external boundaries  $F_B$  is set equal to zero. At internal boundaries  $F^E$  for waves travelling into one domain are prescribed by  $F^E$  for waves travelling out of the other domain. For all other components and interior grid points  $F^E$  follows from  $F^L$ . Each equation can be evaluated in parallel for all the ray ensembles and all grid points, and different frequency bands are only coupled by the source term.

The accuracy of this scheme depends on the relative size of the Eulerian ( $T_E$ ) and Lagrangian ( $T_L$ ) time scales of wave evolution. For  $T_E \ll T_L$  (e.g. a sudden and uniform change in forcing conditions over the entire model grid) the dominant source of error is the low order time integration scheme. If  $T_E \gg T_L$  (e.g. strong energy dissipation at a fixed location, with quasi-stationary boundary conditions and source term) the largest errors may result from spatial interpolation of the source term. Large errors occur if either  $T_E$  or  $T_L$  are comparable to or smaller than  $\Delta t$ . For all cases presented in section 5,  $\Delta t$  is small compared to both  $T_E$  and  $T_L$ . An alternative predictor-corrector scheme was tested, giving results that are indistinguishable from those of the scheme used here.

### 3. THE SOURCE TERM

Previous work by Young and Gorman (1995) and Herbers et al. (2000) suggests that bottom friction is an important dissipation mechanism for energetic swell propagating over a wide continental shelf. Bottom friction was incorporated in our hybrid Eulerian-

Lagrangian model using Tolman's (1994) parametrization of the interaction of waves with a mobile sandy bed, neglecting mean currents and their effects on bedforms. It combines a ripple roughness predictor by Madsen et al. (1990), with Grant and Madsen's (1979) hydrodynamic model, extended to spectral waves by Madsen et al. (1988). For the sheet flow regime Tolman used Wilson's (1989) extrapolation of river flows to oscillatory boundary layers. The source term  $S$  at grid point  $\underline{x}_i$  can be expressed as a quasi-linear function of the energy density  $F^E$  (i.e. eq. (10) with  $R = 0$ ) with an isotropic local decay rate  $\lambda$ :

$$S(\underline{x}_i, f, \theta, t) = \lambda(\underline{x}_i, f, t) \times F^E(\underline{x}_i, f, \theta, t) \quad (13a)$$

$$\lambda(\underline{x}_i, f, t) = -f_e u_b \frac{(2\pi f)^2}{2g \sinh^2(kh_i)} \quad (13b)$$

where  $g$  is the gravity acceleration,  $h_i$  is the local water depth, and  $k$  is the wavenumber magnitude.

$f_e$  is a local dissipation factor that depends on sediment and wave characteristics. The sediment parameters are a representative grain size  $D$ , specific density  $s = \rho_s/\rho$ , where  $\rho_s$  and  $\rho$  are the densities of sediments and water respectively, and the critical Shields number for sediment motion  $\psi_c$ . The wave parameters are representative orbital velocity  $u_b$  and horizontal displacement  $a_b$  at the top of the bottom boundary layer (see appendix A for details).

In order to estimate  $f_e$ , first a skin friction factor  $f'_w$  is determined by solving eqs. (A2) iteratively for a grain roughness  $D$ . The corresponding Shields number  $\psi = f'_w u_b^2 / [g(s-1)D]$  quantifies the movement of sediments and indicates the ripple regime. The equivalent grain roughness  $k_N$  of the bedforms is parameterized as a function of  $\psi$ ,  $\psi_c$ ,  $a_b$ , and  $u_b$ . For  $\psi/\psi_c < 1.2$  (i.e. in the 'relict roughness' regime),  $k_N$  is taken to be 0.01 m. Beyond  $1.2\psi_c$ , in the 'active ripple/sheet flow' regime,  $k_N$  is the sum of a ripple roughness  $k_r$  and a sheet flow roughness  $k_s$  (Eqs. A3). Finally the total friction factor  $f_w$  (skin friction and form drag) is determined by solving eqs. (A2) again using the estimated bedform roughness  $k_N$ , and  $f_e$  is assumed equal to  $f_w$  (e.g. Nielsen, 1992). For  $\psi/\psi_c < 1.2$ ,  $f_e$  is limited to a maximum value of 0.30 (Jonsson, 1980).

The spatial interpolation of the source term onto ray trajectories may cause large errors in the transition region from the 'relict roughness' to the 'active ripple' regime where  $f_e$  increases by one order of magnitude (Figure 3) Tolman (1995) proposed a subgrid model of the source term that accounts for subgrid variations of  $\psi$  resulting from variations over each grid cell of  $h$ ,  $D$ ,  $\psi_c$ , the significant wave height  $H_s$  and peak wave period  $T_p$ . For simplicity these five random variables were assumed to be Gaussian and independent. Because no information on the spatial variability of sediment characteristics was available, a simpler subgrid model was implemented here. If uniform sediment properties are assumed then both  $D$  and  $\psi_c$  are uniform within each grid cell, leaving only three random variables  $h$ ,  $H_s$  and  $T_p$ . In model simulations of swell evolution on the North Carolina shelf, using observed incident wave conditions, most of the subgrid variability of the source term resulted from the subgrid variations of water depths  $h$  rather than the wave parameters  $H_s$  and  $T_p$ , and  $H_s$  was correlated with  $h$ . This predominance of the depth variability was also noted by Tolman (1995) and used in his computations.

In the present subgrid model spatial variations in the water depth  $h$  are represented by

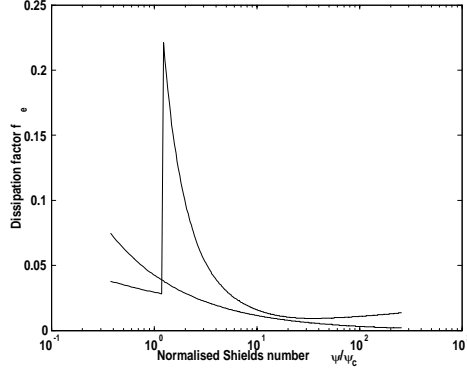


FIG. 3. Example relationships between dissipation factors  $f_e$  and Shields numbers  $\psi$ . The solid line is Tolman's (1994) parameterization for a representative grain size  $D = 0.15$  mm, and wave period  $T = 14$  s. The dashed line shows corresponding values of  $f_e$  using the JONSWAP parameterization.

forming a histogram of depths for a grid cell that consists of the triangles surrounding the grid point  $\underline{x}_i$ , using ten depth bins that span the mean  $\pm 2$  standard deviations of  $h$ . A corresponding linear theory shoaling correction of the wave spectrum is added to account for correlations of  $H_s$  with  $h$ . A subgrid-averaged value of  $\lambda$  is obtained by averaging estimates of  $\lambda$  (for each depth bin, based on the corresponding shoaling-corrected wave spectrum, eq. 13b) weighted by the depth histogram values.

A simpler empirical parameterization of bottom dissipation used in many operational wave prediction models assumes that  $f_e$  is inversely proportional to  $u_b$  so that the factor  $\Gamma = \frac{f_e u_b g}{2}$  is constant and the source term is given by:

$$S(\underline{x}_i, f, \theta, t) = -\Gamma \left[ \frac{2\pi f}{g \sinh(kh_i)} \right]^2 F^E(\underline{x}_i, f, \theta, t) \quad (14)$$

An average value  $\Gamma = 0.038 \text{ m}^2 \text{ s}^{-3}$  was inferred from the JONSWAP North Sea experiment (Hasselmann et al., 1973). This linear ‘JONSWAP’ parameterization (included in the comparisons presented below) yields values of  $f_e$  ( $f_e = 2\Gamma u_b^{-1} g^{-1}$ ) that are close to the movable bed  $f_e$ , except in the active ripple regime, where the JONSWAP parameterization predicts less energy dissipation (Figure 3).

#### 4. MODEL IMPLEMENTATION AND FIELD DATA

The hybrid Eulerian-Lagrangian model (section 2) with a movable bed bottom dissipation source term (section 3) was implemented for the North Carolina shelf region between  $35^\circ \text{ N}$  and  $37^\circ \text{ N}$  (Figure 4). During the DUCK94 experiment a 100 km cross shelf transect of nine bottom mounted pressure sensors was deployed extending from 12 m depth

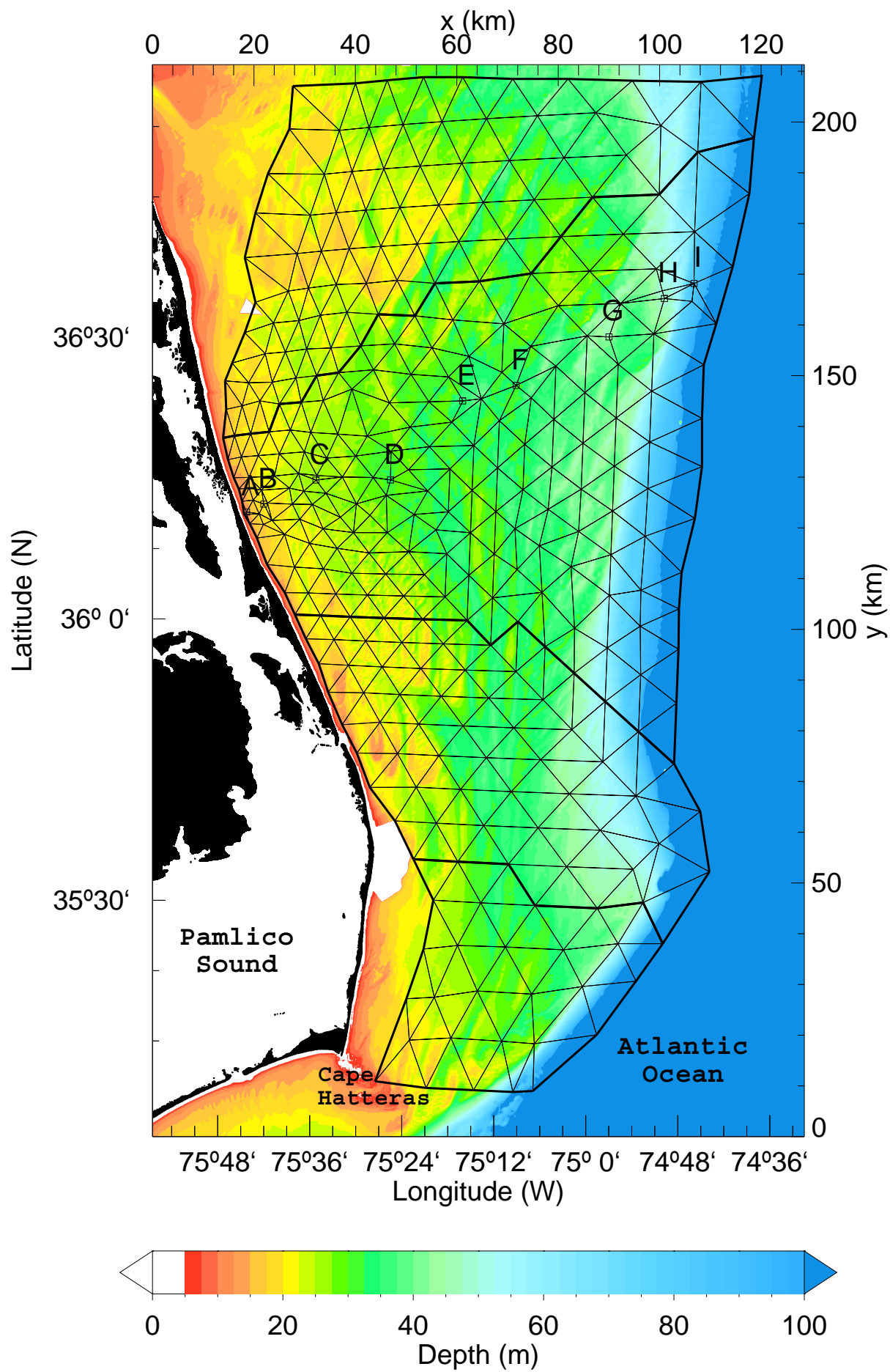


FIG 4.



(site A) to 87 m depth (site I) (Figure 4; Herbers et al. 2000). The instrument deployed at site H in 49 m depth was located within 2 km of 3-m discus buoy 44014 operated by the National Data Buoy Center (NDBC). Between site A and the shore a pressure sensor array was operated in 8 m depth by the Army Corps of Engineers Field Research Facility, Duck, North Carolina. Other instruments on the inner shelf included current meters, thermistors and conductivity sensors in depths ranging from 4 m to 26 m. Data from these instruments show that outside the surf zone the depth-averaged currents are mostly wind-driven with speeds usually in the range 10 to 20  $\text{cm s}^{-1}$ , and occasional stronger currents ( $> 50 \text{ cm s}^{-1}$ ) in storm conditions (Lentz et al., 1999). These currents are generally much weaker than both the wave speeds and the near-bed orbital velocities of energetic swell in shallow water. The effects of currents on the propagation of swell and on the wave bottom boundary layer are neglected here.

Bathymetry data was derived from the National Ocean Service digital database and additional bathymetric surveys conducted during the DUCK94 experiment (Herbers et al., 2000). These data sets were merged and linearly interpolated onto a regular 6" longitude by 6" latitude grid, using a standard Delauney tessellation technique (Figure 4). This grid was then linearly transformed into a Cartesian  $x$  (west-east) and  $y$  (south-north) coordinate grid (resolution 152 and 185 m respectively) that is used in the Lagrangian ray integrations (eqs. 3). Errors introduced by neglecting the curvature of the earth, are small for the size (128 by 211 km) of our domain (O'Reilly and Guza, 1993).

The Eulerian model grid, much coarser than the bathymetry grid, consists of 329 grid points arranged in triangles that vary in size from 5 km on the inner shelf to 10 km on the outer shelf (Figure 4). Slightly coarser grids gave similar results, suggesting that the resolution chosen here is adequate. The model domain was made as small as possible while covering the shelf region through which most of the wave energy, measured by the pressure sensors, has propagated. The model boundaries were chosen to be the 11 m isobath (except around the 8 m array, where a grid point is collocated with the array), the 400 m isobath, and the  $35^{\circ}12'$  N and  $37^{\circ}58'$  N parallels. Swell energy enters the model domain only through the deep water boundary where the spectrum  $F_B(f_j, \theta_l, t)$  is assumed to be spatially uniform. The model domain is subdivided into a main subdomain, around sites A to I and additional subdomains (Figure 4). This allows for the representation of waves coming from high incidence angles, and reduces the memory required to store all the interpolation coefficients, including those for trapped rays, to one gigabyte. Trapped rays are not necessary for the present application, since energy enters the model domain only through the deep water boundary, but were implemented for future applications with other source terms and reflective boundaries. The use of subdomains, described in section 2, introduces some numerical diffusion for waves propagating across the internal boundaries, but these waves, with high incidence angles, carry a very small fraction of the total energy in the present application.

For each grid point  $\underline{x}_i$ , rays are initially traced for 162 frequencies, at arrival direction intervals of  $0.25^{\circ}$ . For each frequency the arrival directions are subsequently bisected (O'Reilly and Guza, 1993) until neighboring rays have directions and positions at the boundary within  $2^{\circ}$  and 5 km of one another, respectively. If the number of rays for a  $3^{\circ}$  sector exceeds 500 the bisection is stopped. The rays are grouped in  $19 \times 120$  bundles, that represent finite bandwidths of the spectrum  $F^E(\underline{x}_i, f_j, \theta_l, t)$  with 19 frequencies  $f_j$  spaced exponentially with a 5% increment from 0.05 Hz to 0.12 Hz, and 120 directions  $\theta_l$

spaced linearly over a full circle with a 3 degree resolution. The number of rays per bundle varies from  $N_f \times 13$  (initial number of rays before bisecting) to  $N_f \times 500$  (an upper limit set for broadly scattered bundles), where  $N_f$  is the number of frequencies per frequency band.  $N_f$  decreases from 9 for 0.05 Hz to 3 for 0.12 Hz.

Wave frequency spectra  $F(f_j, t)$ , integrated over directions, are estimated from the measured bottom pressure records at sites A-I, using a linear theory depth correction. The offshore frequency-direction spectrum  $F_B(f_j, \theta_l, t)$  is estimated by combining the frequency spectrum obtained from the pressure sensor at site H, with directional distributions estimated from the nearby NDBC buoy cross-spectra using the Maximum Entropy Method (Lygre and Krogstad, 1986). This spectrum is back-refracted from site H to deep water, assuming parallel bottom contours, and neglecting the time lag between site H and the offshore model boundary. Although the offshore conditions generally varied slowly on time scales of several hours, this spectrum is determined at 10 minute intervals, in order to match the model time step  $\Delta t$ . Frequency-directional wave spectra on the inner shelf were estimated from the 8 m depth array near site A (Herbers et al., 1999).

Based on core samples collected in 1997 on the inner shelf (Rebecca Beavers, Duke University, personal communication, 1999), and earlier geological data covering the entire shelf (Milliman et al., 1972; Swift and Sears, 1974) we crudely approximate the bottom sediments in the entire area encompassed by the model with a thick uniform layer of fine quartz sand ( $s = 2.65$ ), with a representative grain size  $D = 0.15$  mm and a critical Shields number  $\psi_c = 0.05$ .

The accuracy of the source term interpolation and the representation of refraction in the model is demonstrated with model tests described in Appendix B.

## 5. HINDCASTS

Hindcasts are presented for two time periods in 1994, October 17 through 21 and November 16 through 19, that are representative of fall weather patterns causing large waves on the North Carolina coast. Wind sea and swell were observed in October, generated by a storm that moved across the eastern United States into the North Atlantic, whereas in November large swells arrived from Hurricane Gordon which remained in the western Atlantic, south of Cape Hatteras. In both cases, the model was run both with and without the bottom dissipation source term. Runs without the source term isolate the effects of refraction and shoaling in the evolution of wave spectra, and the difference between runs with and without the source term can be used to assess energy dissipation caused by bottom friction.

### a. October storm

On October 14 and 15 local winds from the north-east were strong enough to contribute significantly to the energy balance on the shelf at the dominant (8-10 s) wave periods (Figure 5). Strong wind forcing is evident at the NDBC buoy where the mean wave direction  $\bar{\theta}$  (defined here as the direction of the first-order moment vector  $\int \int \frac{\underline{k}}{k} F(\underline{k}) dk_x dk_y$ ) follows the local wind direction. As wave generation is not represented in the present model, predictions are not expected to be accurate during the spin-up of this storm.



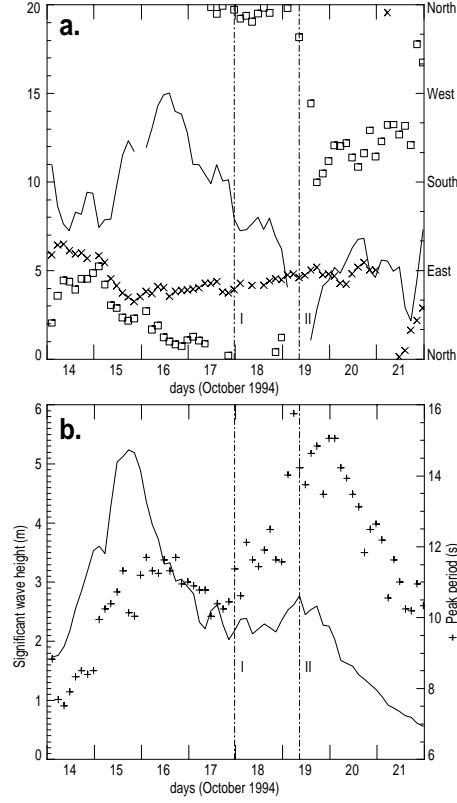


FIG. 4. Three-hour averages of observed wind and wave conditions during the October storm. (a) Wind speed (solid line), wind direction ( $\square$ ), and mean wave direction ( $\times$ ) measured by NDBC buoy 44014 (near site H). (b) Significant wave height and peak period estimated from pressure sensor H (peak periods were replaced by the NDBC buoy values when smaller than 8 s). Vertical dash-dotted lines labeled 'I' (17 October at 23:30 EST) and 'II' (19 October at 08:30 EST) indicate times for which more detailed analyses are presented in Figures 7, 8.

On October 15 the significant wave height observed at site H reached a maximum value  $H_s = 5.3$  m (4.3 m in the restricted model frequency range), with a peak period  $T_p = 11$  s (Figure 5b). After October 16 local winds subsided and  $T_p$  shifted to 15 s, indicating a transition from wind sea to swell. Between October 15 and 18,  $H_s$  decreased to 2.3 m (time I) followed by an increase to 2.8 m on October 19 (time II), with a narrow, swell dominated spectrum (not shown). After October 19  $H_s$  and  $T_p$  gradually decreased to 0.6 m and 10 s respectively.

Model predictions are presented only for the swell-dominated period October 17 to 21. Predictions of  $H_s$  with bottom dissipation are generally in good agreement with observed  $H_s$  on the outer (e.g. Figure 6a) and inner shelf (e.g. Figure 6b). The model predicts the expected turning of  $\bar{\theta}$  towards the shore-normal direction, owing to refraction by the large scale shelf slope (Figure 7). The observed shift in  $\bar{\theta}$ , up to 25 degrees between the offshore buoy and the nearshore (8 m depth) array, is reproduced by the model (Figure 6c). Observed and predicted  $\bar{\theta}$  in 8 m depth differ by less than 5 degrees.

Model predictions without bottom dissipation show a small decrease in wave height across the shelf that is caused by refraction and shoaling effects (Figure 6a,b). The model with movable bed friction predicts a strong attenuation of  $H_s$  across the shelf (Figures 6b, 7) that is comparable to the observed attenuation. The observed and predicted decay across the outer shelf is negligible except for a slight (10%) decrease of  $H_s$  on October 19 when swell energy was maximum (time II in Figure 6a). Strong decay of  $H_s$  is observed and predicted across the inner shelf, up to a factor 2 (equivalent to a 75% energy reduction) (Figure 6b). The observed and predicted decrease of  $H_s$  across the shelf is generally smaller when  $H_s$  is smaller (e.g. compare times I and II in Figures 6a, 6b). On October 21 when  $H_s$  was less than 0.5 m, the observed and predicted  $H_s$  (with and without bottom dissipation) are nearly uniform across the shelf.

Details of the representation of bottom friction in the model are illustrated in Figure 8. The predicted variation of the dissipation factor  $f_e$  on the scale of the grid resolution confirms the importance of subgrid modelling of the movable bed (Tolman, 1995). Predicted boundary layer regimes (relict roughness or active ripples) are sensitive to the offshore wave conditions. On October 17 (time I in Figures 5, 6), the model predicts relict roughness over most of the shelf with dissipation factors  $f_e$  close to the relict regime minimum ( $f_e = 0.04$ ) and a sharp transition to active ripples ( $0.08 < f_e < 0.18$ ) in depths shallower than 25 m (Figure 8a). The boundary between active and relict ripples generally follows the depth contours. The corresponding local decay rate  $|\lambda| \propto f_e u_b \sinh^{-2}(kh)$  (eqs. 13b, A1a) is enhanced not only by the large increase in  $f_e$ , but also by the increase of the bottom orbital velocity  $u_b$  in shallow water. Seaward of site D, predicted  $H_s$  with and without bottom dissipation are nearly equal to the observed  $H_s$ , whereas further inshore, predicted  $H_s$  with and without bottom dissipation diverge sharply and predictions of  $H_s$  with bottom dissipation reproduce the observed decay of  $H_s$  across the inner shelf (Figure 8b). The strongly enhanced dissipation predicted by the movable bed model on the inner shelf is consistent with the observed variations in wave heights. However, the JONSWAP parameterization also gives reasonable predictions of  $H_s$  in this case.

On October 19 when the swell energy was maximum (time II in Figures 5, 6), the movable bed model predicts active ripples on the entire shelf (Figure 8c). The corresponding values of  $f_e$  are maximum close to the shelf break ( $0.1 < f_e < 0.12$ ), and decrease inshore ( $f_e = 0.04$  at site B). A strong decay of wave energy inshore of site G is evident in

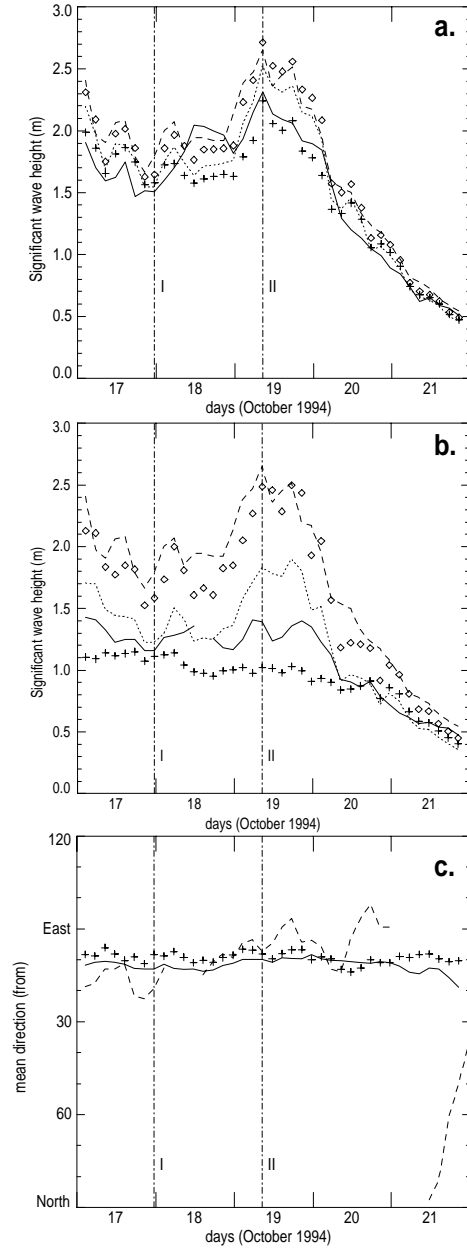


FIG. 5. Three-hour averages of observed (solid line) and predicted (+: with movable-bed source term,  $\diamond$ : without) significant wave heights at sites F (a) and B (b) after the October storm. The dotted lines represent model results at the same sites based on the JONSWAP linear damping formulation. The offshore  $H_s$  is indicated with a dashed line. (c) The mean wave direction  $\bar{\theta}$  measured at the 8 m depth array (solid line) is compared to the model prediction with the movable bed source term (+). The offshore  $\bar{\theta}$  is indicated with a dashed line. Vertical dash-dotted lines labeled 'I' and 'II' indicate times for which more detailed analyses are presented in Figures 7, 8.

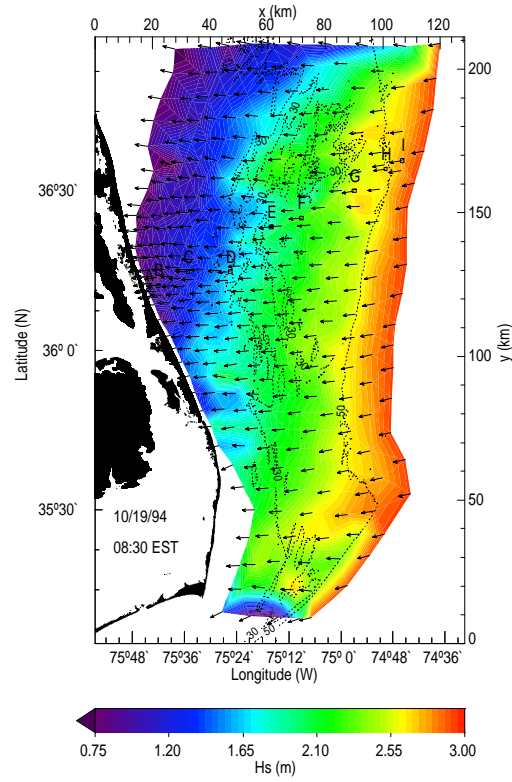


FIG. 6. Model predictions (with movable bed source term) of significant wave height (colors) and mean wave direction (arrows) at time II (Figures 5, 6). Dotted lines indicate the 30 m and 50 m isobaths.

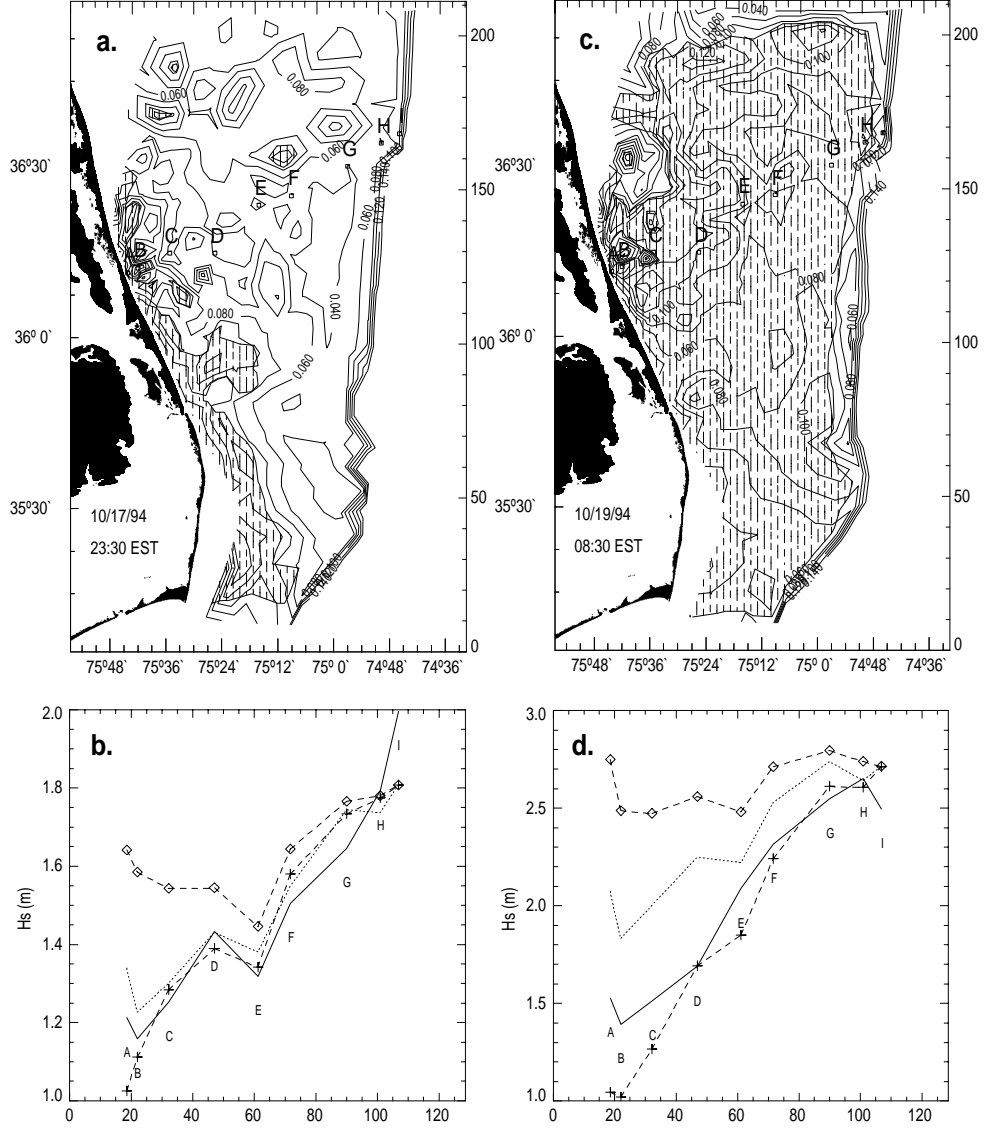


FIG. 7. (a) Ripple regime based on local mean water depth (hatched for active ripples, blank for relict roughness), and dissipation factor  $f_e$  (contour interval is 0.02) at time 'I' (Figures 5, 6). (b) Observed (solid line) and predicted ( $\diamond$ : without bottom dissipation,  $+$ : with movable-bed source term, dotted: with JONSWAP source term)  $H_s$  at time I, as a function of cross-shelf distance. (c) Same as (a) for time II (Figures 5, 6). (d) Same as (b) for time II.

the difference between model predictions of  $H_s$  with and without bottom dissipation and these energy losses (on average  $0.35 \text{ W m}^{-2}$  over the entire shelf) are consistent with the observations (Figure 8d). Inshore of site D the model with the source term underpredicts  $H_s$  (overpredicts decay) by about 25 to 50 cm. The JONSWAP parameterization on the other hand overpredicts  $H_s$  by 40 to 60 cm, as might be expected from figure 3.

## b. Hurricane Gordon

Although the eye of Hurricane Gordon remained south of Cape Hatteras, local winds were strong ( $10\text{--}15 \text{ m s}^{-1}$ ) on November 17 through the morning of November 18 (Figure 9a). During the peak of this event (time III) when  $H_s \simeq 10 \text{ m}$  and  $T_p \simeq 15 \text{ s}$  (Figure 9a), the local wind speed was about  $13 \text{ m/s}$  and the mean wave and wind direction differed by about 30 degrees. Estimated values of the wind energy input in the model frequency band (The WAMDI Group, 1988, eq. (2.9)) are below  $2 \text{ W m}^{-2}$  on most of the shelf, while the predicted bottom dissipation rate is generally between 2 and  $10 \text{ W m}^{-2}$  (both terms are maximum near the coast). Hence, although bottom dissipation appears to be the dominant source term, neglecting the wind input in this case may cause significant errors.

At time III the model predicts a gradual turning of the mean wave direction from  $115^\circ$  in deep water to  $88^\circ$  in 8 m depth (Figure 10), in good agreement with the mean direction ( $88^\circ$ ) observed at the 8 m array (not shown). Model predictions without bottom dissipation yield a decrease in  $H_s$  from 8.5 m at site I near the shelf break to 7.4 m at site B on the inner shelf. This attenuation, associated with the time evolution of the storm and conservative shoaling and refraction processes, accounts for only part of the observed decrease of  $H_s$  to 5.8 m at site B. Including movable bed dissipation brings the model in better agreement with the observations (Figure 11b). The predicted values of the dissipation factor  $f_e$  are about 10 times smaller than the values for the October event, owing to larger Shields numbers. On most of the shelf,  $f_e$  predictions vary between 0.01 and 0.02 (Figure 11a), corresponding to sheet flow. Active ripples are predicted close to the shelf break in depths greater than 40 m. The representative bottom velocity  $u_b$  (a linear function of  $H_s$  for a given spectral shape) is 3 times larger than in the October event. In an absolute sense, the dissipation rate  $|S|$  (proportional to  $f_e u_b^3$ ; eqs. (13)) is a factor 3 larger than in the October event, but the relative decay rate  $|\lambda|$  (proportional to  $f_e u_b$ ; eq. (13b)) is a factor 3 smaller. As a result, the predicted relative decay of  $H_s$  across the shelf, due to bottom dissipation, is weaker for the Hurricane Gordon case than the October swell event (a 14% decrease compared to 36% in October, cf. figures 8d and 11b). The JONSWAP parameterization yields  $H_s$  predictions for Hurricane Gordon, that are close to both observed  $H_s$  and movable bed predictions (Figure 11b).

## 6. DISCUSSION

### a. Movable bed model

The comparisons between observations and model predictions suggest that the observed decay of swell energy across the shelf is primarily the result of refraction and energy dissipation.

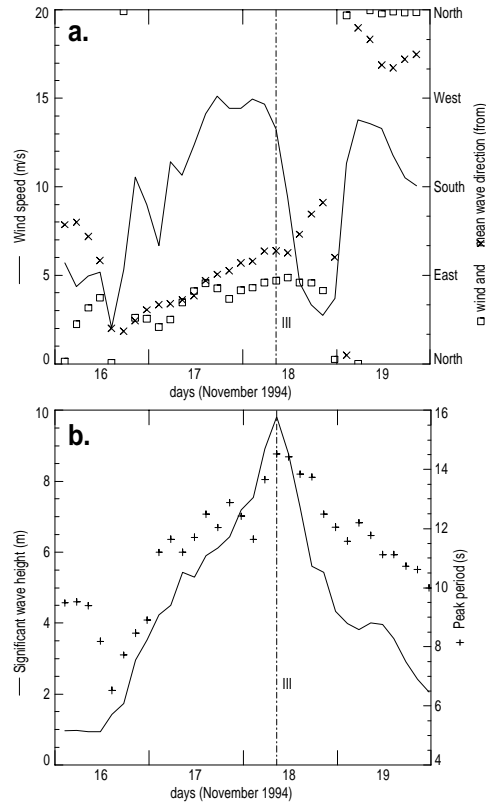


FIG. 8. Wind and wave conditions during Hurricane Gordon (same format as Figure 5). The vertical dash-dotted line labeled 'III' (18 November at 08:30 EST) indicates the time when  $H_s$  was maximum offshore.

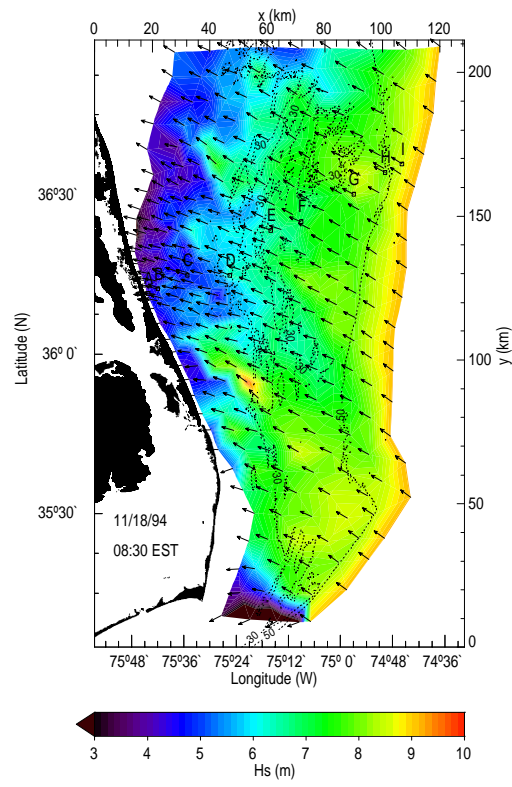


FIG. 9. Model predictions (with moveable bed source term) of significant wave height (colors) and mean wave direction (arrows) at the peak of Hurricane Gordon (time ‘III’ in Figure 9). Dotted lines indicate the 30 m and 50 m isobaths.



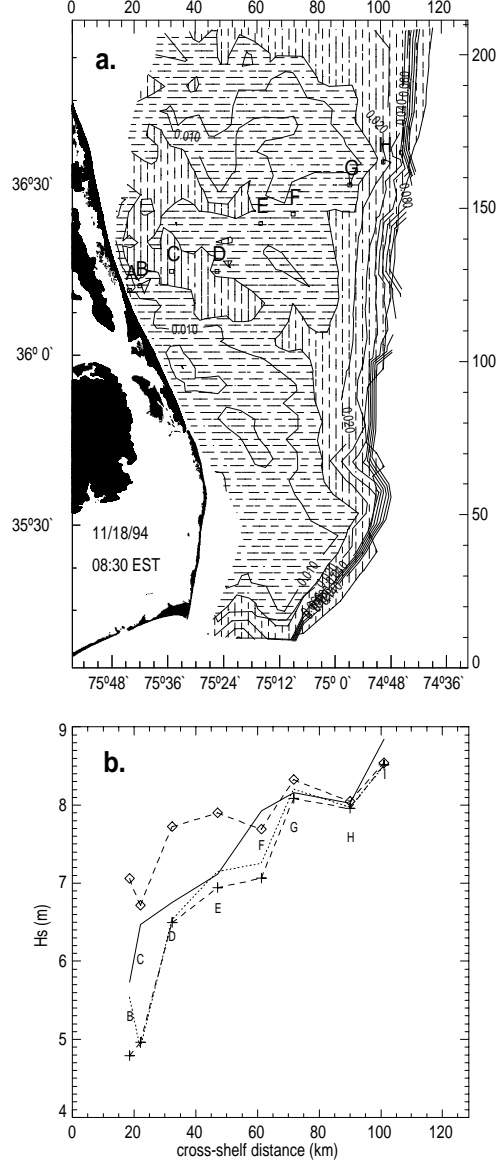


FIG. 10. Ripple regimes, dissipation factors and wave height comparison at the peak of Hurricane Gordon (time ‘III’ in Figure 9). Same format as figure 8, with the addition of the  $f_e = 0.01$  contour, and horizontal hatches for sheet flow conditions determined from the threshold criterion  $\psi_{sf} = 0.172D^{-0.376}$  where  $D$  is in cm (Li and Amos, 1999).

pation in the boundary layer over a movable sandy bed. Predicted wave frequency spectra (not shown) are also in good agreement with observed spectra, except at very low frequencies ( $f < 0.06$  Hz) where energy levels are relatively low. The hindcast results suggest large spatial and temporal variations of the dissipation factor  $f_e$  as the seabed transitions through different roughness regimes (Figure 3). Tests with different sand grain sizes in the range of probable values for the region (0.15 to 0.2 mm) indicated little sensitivity of the results. Although more accurate offshore wave data and detailed sediment distributions are needed for comprehensive tests of the bed roughness parameterization, the present results show a model tendency to overpredict swell damping, in particular in the active ripple regime (Figures 6 and 8.d). The parameterization of the ripple roughness  $k_r$  was tuned to reproduce laboratory experiments with irregular but unidirectional waves (Madsen et al., 1990). Field conditions, with directionally spread waves, are likely to generate more irregular and less steep ripples, with smaller roughness  $k_r$ , than laboratory experiments (e.g. Nielsen, 1981). Therefore the estimates of  $k_r$  may be biased high. A reduction of  $k_r$  by 30% significantly improved the model accuracy (not shown).

The JONSWAP parameterization gives a relative decay in wave height  $H/H_{offshore}$  that is constant for a given dominant frequency. The observations presented here, all for swell with a peak period  $T_p \simeq 15$  s, instead show a variable relative decay, in response to changes in the wave height (e.g. Figure 6.b). Equivalent values of  $\Gamma$ , the JONSWAP coefficient, were inferred from the movable-bed model hindcasts. At site F on the outer shelf, we find  $0.025 \text{ m}^2\text{s}^{-3}$ ,  $0.11 \text{ m}^2\text{s}^{-3}$ , and  $0.050 \text{ m}^2\text{s}^{-3}$  at times I, II and III respectively. For the same times at site B on the inner shelf,  $\Gamma$  values are  $0.11 \text{ m}^2\text{s}^{-3}$ ,  $0.095 \text{ m}^2\text{s}^{-3}$ , and  $0.057 \text{ m}^2\text{s}^{-3}$  respectively. These values generally fall between the JONSWAP average value  $\Gamma = 0.038 \text{ m}^2\text{s}^{-3}$ , and the one obtained from observations in the Great Australian Bight (Young and Gorman, 1995),  $\Gamma = 0.152 \text{ m}^2\text{s}^{-3}$ . Although the JONSWAP formulation with the widely used value  $\Gamma = 0.038 \text{ m}^2\text{s}^{-3}$  gives reasonable wave height predictions in most conditions (Figures 6, 8 and 11), it cannot reproduce the observed variations in swell decay, and significantly overestimates wave heights in active ripple conditions, as was also noticed by Weber (1991a). In contrast the constant roughness ( $k_N = 4$  cm) proposed by Weber (1991) yields values of  $H_s$  that are still too high (by 30 cm) in the October 19 case, but too low (by 2.5 m) in the November 18 case (not shown). The movable bed model, adopted from Tolman (1994) without any adjustments, captures this variability, and fine tuning of all the empirical parameters, should further improve swell predictions. However, the movable bed parameterization requires site-specific sediment data that are not always available. Without such data, operational wave models may be better off with more robust dissipation models (e.g. Weber, 1991a; Tolman, 1994; Luo and Monbaliu, 1994; Young and Gorman, 1995).

## b. model efficiency

The new hybrid Eulerian-Lagrangian model CREST, presented here, was used to investigate the effects of a movable sandy sea bed on the transformation of swell across a continental shelf. Other physical processes such as wave generation, resonant non linear interactions between waves (Hasselmann, 1962) and resonant Bragg scattering of waves by bottom features (Long, 1973) can be incorporated as additional source terms in the

energy balance equation. Hence the present model provides an alternative to the Eulerian finite difference scheme models commonly used for wave prediction. With  $N_{\Delta t}$  a typical number of time steps for a ray bundle, and  $N_s$  a typical number of interpolation coefficients  $A_{il}^n$  and  $B_{il}^n$  for a given time step, the CREST wave model requires memory space for storing the interpolation coefficients that is a factor  $N_{\Delta t} \times N_s$  (of the order of 200 in the calculations presented here) larger than the space used for storing the spectrum. Thus CREST requires much more memory per grid point than an Eulerian model, that only needs to store the spectrum. The hybrid approach is attractive for applications where the spatial scales  $L_S$  of variations in the source terms are much larger than spatial scales  $L_R$  of refraction effects. An Eulerian model describing refraction with a finite difference scheme in space requires a grid resolving both  $L_R$  and  $L_S$  whereas the Eulerian grid in the present model needs to resolve only  $L_S$  because  $L_R$  is resolved by the precomputed rays. If  $L_S$  is much greater than  $L_R$  this property reduces drastically the number  $N_{gp}$  of grid points required for an accurate integration of the energy balance equation. Reducing  $N_{gp}$  has the added benefit that in coarser grids fewer grid points are used to interpolate of the source term for a given ray bundle, thus of reducing the number  $N_s$  of interpolation coefficients per time step. The implementation of an Eulerian finite difference scheme with a resolution of about 500 m would have similar memory needs as the calculations presented here.

The considerable memory burden imposed by the storage of the ray information can be reduced by dividing the model domain into subdomains. The use of subdomains is clearly a compromise between a pure Lagrangian advection scheme and practical considerations. At the internal boundaries it re-introduces numerical diffusion in the advection and recouples the rays to the grid for  $\tau > 0$ . Although not necessary in the application presented here it seems unavoidable for implementations of CREST on very large areas ( e.g.  $> 10^6 \text{ km}^2$ ).

The representation by refraction alone of the effects of small scale bottom irregularities is cumbersome in the present model, and may not reflect the entire complexity of that process. A statistical representation of the interaction of waves with the smallest scale bathymetric features (e.g. the wave-bottom Bragg scattering source term described in Hasselmann (1966), and Long (1973)) appears attractive because it would improve the physical description of wave-bottom interactions and the rays computed on smoother bathymetry would be less scattered thus requiring a smaller number  $N_s$  of interpolation coefficients.

The small number of grid points in CREST is also advantageous for complex source terms (e.g. quartet interactions between wave components) that are prohibitively expensive to evaluate accurately on a high-resolution grid. Furthermore the flexible model grid generated from any arbitrary set of points can be tailored to the bathymetry and shape of the model domain with higher resolution in the shallowest parts of the domain. In this respect CREST is similar to the TOMAWAC model (Benoit et al., 1996).

For practical applications, computing ray trajectories is too expensive to allow a time-dependent ray geometry. This prevents the use of CREST in regions with strong temporal medium variations such as unsteady currents and tidal depth changes found in shallow estuaries and macrotidal seas, unless an approximate representation of these effects as source terms is found.

## 7. SUMMARY

A non-stationary spectral wave model was developed using a hybrid Eulerian-Lagrangian scheme to examine the damping of swell propagating across a wide, shallow continental shelf. The model accurately represents refraction by advecting wave energy from deep water along a full spectrum of precomputed ray trajectories to a large number of grid points on the shelf. The source term in the energy balance is computed at each of these grid points, based on the complete frequency-directional spectrum. The source term is then interpolated from the Eulerian grid onto the rays, thus allowing for nonlinear coupling of wave components traveling along different rays. The energy balance is averaged over ensembles of rays to represent a finite spectral bandwidth. The (Lagrangian) computation of energy advection along rays and the (Eulerian) source term evaluation are carried out in parallel through the entire model domain. Source term formulations can be adapted from existing third-generation wave prediction models, whereas the finite difference propagation schemes of these models are replaced with a full Lagrangian ray method. This hybrid scheme avoids the numerical diffusion and ‘garden sprinkler’ problems of existing models that use finite difference schemes. The ray calculations and source term interpolation scheme add considerable computational effort, but both the ray trajectories and interpolation coefficients are precomputed for a given coastal region and model grid. The spectral energy balance is integrated in time with an efficiency comparable to existing finite-difference schemes.

The model was implemented with a source term restricted to energy dissipation in the bottom boundary layer over a movable sandy bed, as parameterized by Tolman (1994). The model was used to hindcast swell evolution across the North Carolina continental shelf for a range of wave conditions (significant wave heights between 0.5 and 10 m, and peak periods between 8 and 17 s) observed during two storms in 1994. Good agreement between observed and predicted variations of significant wave heights and mean wave directions across the shelf supports the hypothesis that refraction and movable bed bottom friction dominate the evolution of swell over a shallow sandy continental shelf.

*Acknowledgments.* This research is supported by the Coastal Dynamics Program of the Office of Naval Research and by the French Navy Hydrographic and Oceanographic Service. The DUCK94 field data were collected by staff from the Scripps Institution of Oceanography-Center for Coastal Studies and the Naval Postgraduate School. Paul Jessen contributed significantly to the wave and bathymetry data analysis. Wave data were provided by the Field Research Facility of the U.S. Army Corps of Engineers Waterways Experiment Station’s Coastal Engineering Research Center and the National Data Buoy Center. Permission to use these data is appreciated. We are thankful to Timothy Stanton, Edward Thornton and Hendrik Tolman for fruitful discussions, and anonymous reviewers for constructive remarks.

## Appendix A

### PARAMETERIZATION OF THE BOTTOM BOUNDARY LAYER

The bulk amplitudes of wave orbital velocity  $u_b$  and displacement  $a_b$  at the top of the bottom boundary layer are evaluated using equations (11) and (25) in Madsen et al.'s (1988) model:

$$u_b^2 = \int_{\underline{k}} \frac{8\pi^2 f^2}{\sinh^2(kh)} F(\underline{k}) d\underline{k} \quad (\text{A1a})$$

$$a_b^2 = \int_{\underline{k}} \frac{2}{\sinh^2(kh)} F(\underline{k}) d\underline{k} \quad (\text{A1b})$$

For a linear profile of eddy viscosity, Grant and Madsen (1979) determined the skin friction factor  $f'_w$  and total friction factor  $f_w$  (ratio of bulk stress and  $u_b^2$ ) as implicit functions of the grain size  $D$  and equivalent grain roughness of the bedforms  $k_N$ , respectively:

$$\frac{z_0}{l} = \sqrt{\frac{2}{f'_w \text{ or } f_w} \frac{D \text{ or } k_N}{30\kappa a_b}} \quad (\text{A2a})$$

$$f'_w \text{ or } f_w = \frac{\kappa^2}{2 \left( \ker^2 \left( 2\sqrt{z_0/l} \right) + \text{kei}^2 \left( 2\sqrt{z_0/l} \right) \right)} \quad (\text{A2b})$$

where  $z_0/l$  is an adimensional roughness length,  $\kappa$  is Von Karman's constant ( $\kappa = 0.4$  for clear water), and  $\ker$  and  $\text{kei}$  are the zeroth order Kelvin functions.

In the presence of active ripples or sheet flow,  $k_N$  is taken to be the sum of a ripple roughness  $k_r$  and a sheet flow roughness  $k_s$ . Madsen et al. (1990) gave empirical values of  $k_r$  for random waves in laboratory experiments and Wilson (1989) extrapolated to waves values of  $k_s$  measured for river flows:

$$k_r = a_b \times 1.5 \left( \frac{\psi}{\psi_c} \right)^{-2.5} \quad (\text{A3a})$$

$$k_s = 0.57 \frac{u_b^{2.8} a_b^{-0.4}}{[g(s-1)]^{1.4} (2\pi)^2} \quad (\text{A3b})$$

## Appendix B

### MODEL TESTS

The error in the ray computation is controlled by the variable time step, but other errors are introduced by the discretization in frequency and direction and the ray ensemble average. The accuracy of the propagation scheme was tested by applying the model with the source term set equal to zero to an idealized shelf with parallel depth contours, for a uniform and stationary offshore boundary condition (Figure 12.a) . The mean wave directions and directional distributions of energy predicted by the model agree closely with analytical (Snel's law) results (Figure 12.b and 12.c), demonstrating that ray integration and discretization errors are small.

The model formulation assumes that the source term varies on scales comparable to or larger than the spacing of the grid. This condition is required for a valid interpolation. The accuracy of the interpolation scheme was tested by computing the source term directly at 20 additional grid points located along a ray segment (for 0.07 Hz waves) that covers a full source term integration time step  $\Delta t = 600$  s. Source term estimates interpolated onto this ray segment with eqs. (12d,e) in a hindcast of wave evolution across the North Carolina shelf (section 5), are compared with direct estimates at the additional grid points in Figure 13 . Results (averaged over a time step  $\Delta t$ ) show that the linear spatial interpolations give a good approximation of subgrid variations in the source term. That is, the source term gradients are rather well resolved by the grid. The interpolation is most accurate when the ripple regime is the same at all the neighboring grid points. Overall, a quasi-linear implementation of the movable bed source term (i.e.  $S = \lambda F$ ,  $R = 0$  in eq. (10)) (Figure 13.a), yields smaller errors than a non-linear implementation of the same source term (i.e.  $\lambda = 0$ ,  $R = S$  in eq. (10)) (Figure 13.b).

### REFERENCES

- Benoit, M., F. Marcos, and F. Becq, 1996: Development of a third generation shallow-water wave model with unstructured spatial meshing. *Proceedings of the 25th international conference on coastal engineering*, ASCE, 465–478.
- Booij, N., R. C. Ris, and L. H. Holthuijsen, 1999: A third-generation wave model for coastal regions. 1. model description and validation. *J. Geophys. Res.*, **104**(C4), 7,649–7,666.
- Bouws, E. and J. A. Battjes, 1982: A Monte-Carlo approach to the computation of refraction of water waves. *J. Geophys. Res.*, **87**(C8), 5,718–5,722.
- and G. J. Komen, 1983: On the balance between growth and dissipation in an extreme depth-limited wind-sea in the southern North Sea. *J. Phys. Oceanogr.*, **13**, 1653–1658.
- Cavaleri, L. and P. Malanotte-Rizzoli, 1981: Wind wave prediction in shallow water: theory and applications. *J. Geophys. Res.*, **86**(C5), 10,961–10,975.

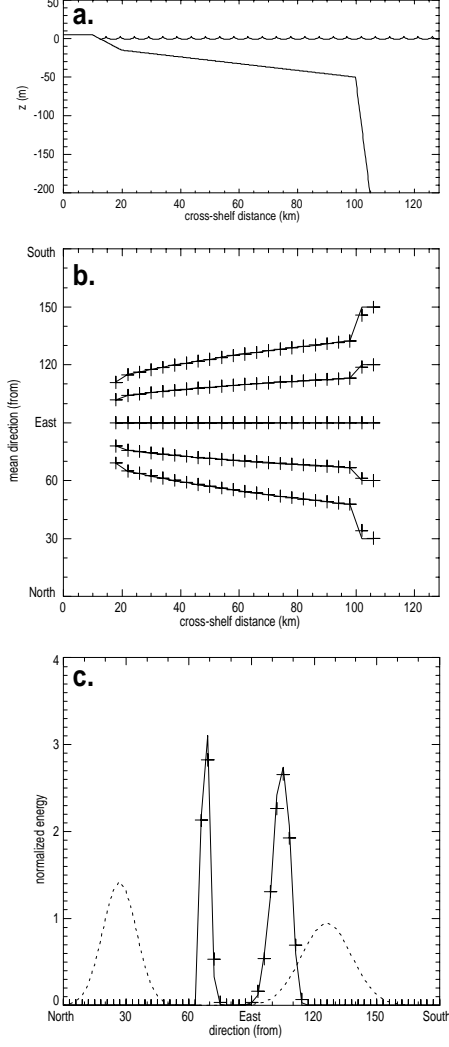


FIG. 11. Model tests with an alongshore uniform shelf. The offshore wave energy is distributed uniformly over a narrow (0.0655-0.0685 Hz) frequency band. (a) Cross-shelf depth profile. (b) Predicted (+) and analytical (solid line) mean wave direction versus cross-shelf distance. Results are shown for narrow offshore directional distributions (standard deviation of 10 degrees) with mean wave directions varying between  $30^\circ$  and  $150^\circ$ . (c) An example directional distribution predicted by the model (+) in 20 m depth for a given offshore bimodal distribution (dotted line) is compared to the analytical solution (solid line).

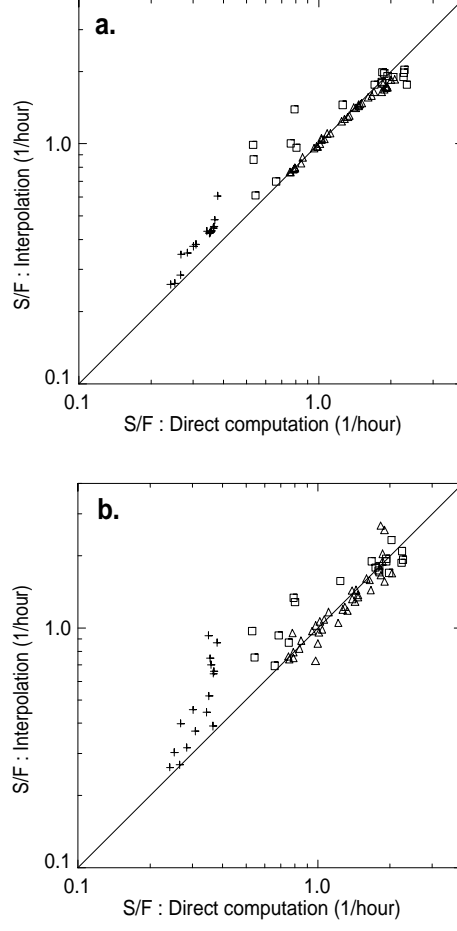


FIG. 12. Interpolated versus directly computed values of  $S/F$  (inverse of the bottom dissipation e-folding time), using (a) a quasi-linear source term implementation that interpolates  $\lambda$  (Eq. 13b), and (b) a non-linear implementation of the same source term that interpolates  $S$  (Eq. 13a). The source term estimates are averages over a 10 minute time step. Symbols represent different boundary layer regimes within the grid cell: relict ripples (+), active ripples ( $\Delta$ ), and a transition from relict to active ripples ( $\square$ ).



- Clifton, H. E., 1976: Wave-formed sedimentary structures: a conceptual model. *Beach and nearshore sedimentation*, R. A. Davis, Jr et R. L. Ethington, Eds., number 24, SEPM, 126–148.
- Dobson, R. S., 1967: Some applications of a digital computer to hydraulic engineering problems. Technical Report 80, Department of Civil Engineering, Stanford University.
- Gelci, R., H. Cazalé, and J. Vassal, 1957: Prévision de la houle. la méthode des densités spectroangulaires. *Bulletin d'information du Comité central d'Océanographie et d'Etude des Côtes*, **9**, 416–435.
- Graber, H. C. and O. S. Madsen, 1988: A finite-depth wind-wave model. part 1: model description. *J. Phys. Oceanogr.*, **18**, 1,465–1,483.
- Grant, W. D. and O. S. Madsen, 1979: Combined wave and current interaction with a rough bottom. *J. Geophys. Res.*, **84**, 1797–1808.
- and ———, 1982: Movable bed roughness in unsteady oscillatory flow. *J. Geophys. Res.*, **87**(C1), 469–481.
- Hasselmann, K., 1962: On the non-linear energy transfer in a gravity wave spectrum, part 1: general theory. *J. Fluid Mech.*, **12**, 481–501.
- , 1966: Feynman diagrams and interaction rules of wave-wave scattering processes. *Review of Geophysics*, **4**(1), 1–32.
- , T. P. Barnett, E. Bouws, H. Carlson, D. E. Cartwright, K. Enke, J. A. Ewing, H. Gienapp, D. E. Hasselmann, P. Kruseman, A. Meerburg, P. Müller, D. J. Olbers, K. Richter, W. Sell, and H. Walden, 1973: Measurements of wind-wave growth and swell decay during the Joint North Sea Wave Project. *Deut. Hydrogr. Z.*, **8**(12), 1–95. Suppl. A.
- Herbers, T. H. C., S. Elgar, and R. T. Guza, 1999: Directional spreading of waves in the nearshore. *J. Geophys. Res.*, **104**(C4), 7683–7693.
- , E. J. Hendrickson, and W. C. O'Reilly, 2000: Propagation of swell across a wide continental shelf. *J. Geophys. Res.* In press.
- Jonsson, I. G., 1980: A new approach to oscillatory rough turbulent boundary layers. *Ocean Eng.*, **7**, 109–152.
- Kajiura, K., 1968: A model of the bottom boundary layer in water waves. *Bull. Earthquake Res. Inst. Univ. Tokyo*, **46**, 75–123.
- Komen, G. J., L. Cavaleri, M. Donelan, K. Hasselmann, S. Hasselmann, and P. A. E. M. Janssen, 1994: *Dynamics and modelling of ocean waves*. Cambridge University Press, Cambridge.
- Lentz, S., R. T. Guza, S. Elgar, F. Feddersen, and T. H. C. Herbers, 1999: Momentum balances on the North Carolina inner shelf. *J. Geophys. Res.*, **104**(C8), 18,205–18,226.

- Li, M. Z. and C. L. Amos, 1998: Predicting ripple geometry and bed roughness under combined waves and currents in a continental shelf environment. *Continental Shelf Research*, **18**, 941–970.
- and ———, 1999: Sheet flow and large wave ripples under combined waves and currents: field observations, model predictions and effect on boundary layer dynamics. *Continental Shelf Research*, **19**, 637–663.
- Long, R. B., 1973: Scattering of surface waves by an irregular bottom. *J. Geophys. Res.*, **78**(33), 10,987–11,004.
- Longuet-Higgins, M. S., 1957: On the transformation of a continuous spectrum by refraction. *Proceedings of the Cambridge philosophical society*, **53**(1), 226–229.
- Luo, W. and J. Monbaliu, 1994: Effects of the bottom friction formulation on the energy balance for gravity waves in shallow water. *J. Geophys. Res.*, **99**(C9), 18,501–18,511.
- Lygre, A. and H. E. Krogstad, 1986: Maximum entropy estimation of the directional distribution in ocean wave spectra. *J. Phys. Oceanogr.*, **16**, 2,052–2,060.
- Madsen, O. S., Y.-K. Poon, and H. C. Graber, 1988: Spectral wave attenuation by bottom friction: theory. *Proceedings of the 21th international conference on coastal engineering*, ASCE, 492–504.
- , P. P. Mathisen, and M. M. Rosengaus, 1990: Movable bed friction factors for spectral waves. *Proceedings of the 22nd international conference on coastal engineering*, ASCE, 420–429.
- Mathisen, P. P. and O. S. Madsen, 1999: Wave and currents over a fixed rippled bed. 3. bottom and apparent roughness for spectral waves and currents. *J. Geophys. Res.*, **104**(C8), 18,447–18,461.
- Milliman, J. D., O. H. Pilkey, and D. A. Ross, 1972: Sediments of the continental margin off the eastern United States. *Geological Society of America Bulletin*, **83**, 1315–1333.
- Munk, W. H. and M. A. Traylor, 1947: Refraction of ocean waves: a process linking underwater topography to beach erosion. *Journal of Geology*, **LV**(1), 1–26.
- Nielsen, P., 1981: Dynamics and geometry of wave-generated ripples. *J. Geophys. Res.*, **86**(C7), 6,467–6,472.
- , 1992: *Coastal bottom boundary layers and sediment transport*. World Scientific Publishing.
- O'Reilly, W. C. and R. T. Guza, 1991: Comparison of spectral refraction and refraction-diffraction wave models. *Journal of Waterway, Port, Coastal and Ocean Engineering*, **117**(3), 199–215.
- and ———, 1993: A comparison of two spectral wave models in the Southern California Bight. *Coastal Eng.*, **19**, 263–282.

- Press, W. H., S. A. Teukolsky, W. T. Vetterling, and B. P. Flannery, 1992: *Numerical Recipes*. Cambridge University Press, second edition.
- Shemdin, O. H., S. V. Hsiao, H. E. Carlson, K. Hasselmann, and K. Schulze, 1980: Mechanisms of wave transformation in finite depth water. *J. Geophys. Res.*, **89**(C9), 5012–5018.
- Sobey, R. J., 1986: Wind-wave prediction. *Annu. Rev. Fluid Mech.*, **18**, 149–172.
- SWAMP Group, 1984: *Ocean wave modelling*. Plenum Press, New York.
- Swift, D. J. P. and P. Sears, 1974: Estuarine and littoral depositional patterns in the surficial sand sheet central and southern Atlantic shelf of North America. *Mémoires de l'Institut Géologique du Bassin Aquitain*, **7**, 171–189.
- Tolman, H. L., 1994: Wind waves and moveable-bed bottom friction. *J. Phys. Oceanogr.*, **24**, 994–1,009.
- , 1995: Subgrid modeling of moveable-bed bottom friction in wind wave models. *Coastal Eng.*, **26**, 57–75.
- Traykovski, P., A. E. Hay, J. D. Irish, and J. F. Lynch, 1999: Geometry, migration, and evolution of wave orbital ripples at LEO-15. *J. Geophys. Res.*, **104**(C1), 1,505–1,524.
- WAMDI Group, 1988: The WAM model - a third generation ocean wave prediction model. *J. Phys. Oceanogr.*, **18**, 1,775–1,810.
- Weber, N., 1991a: Bottom friction for wind sea and swell in extreme depth-limited situations. *J. Phys. Oceanogr.*, **21**, 149–172.
- Weber, S. L., 1988: The energy balance of finite depth gravity waves. *J. Geophys. Res.*, **93**, 3,601–3,607.
- , 1991b: Eddy-viscosity and drag-law models for random ocean wave dissipation. *J. Fluid Mech.*, **232**, 73–98.
- Whitham, G. B., 1974: *Linear and nonlinear waves*. Wiley, New York. 636 p.
- Wiberg, P. L., 1995: A theoretical investigation of boundary layer flow and bottom shear stress for smooth, transitional and rough flow under waves. *J. Geophys. Res.*, **100**(C11), 22,667–22,679.
- and C. K. Harris, 1994: Ripple geometry in wave-dominated environments. *J. Geophys. Res.*, **99**(C1), 775–789.
- Wilson, K. C., 1989: Friction of wave-induced sheet flow. *Coastal Eng.*, **12**, 371–379.
- Young, I. R., 1988: A shallow water spectral wave model. *J. Geophys. Res.*, **93**(C5), 5,113–5,129.
- and R. M. Gorman, 1995: Measurements of the evolution of ocean wave spectra due to bottom friction. *J. Geophys. Res.*, **100**(C6), 10,987–11,004.

Fig. 4: Bottom topography and model grid. The grid points where the source term is evaluated are the nodes of the triangular mesh. A linear interpolation is applied in each triangle to approximate the source term along the rays (Figure 1). The entire model domain is subdivided into subdomains separated by thicker lines. Grid points denoted with dots labeled A to I are the locations of pressure sensors deployed during the DUCK94 field experiment.